Pergamon

Geochimica et Cosmochimica Acta, Vol. 66, No. 4, pp. 713–728, 2002

0016-7037/−1898 $22.00 + .00

PII S0016-7037(01)00797-9

Experimental study of incongruent evaporation kinetics of enstatite in vacuum and in hydrogen gas

SHOGO TACHIBANA,[1,2] AKIRA TSUCHIYAMA,[1] and HIROKO NAGAHARA[2]

[1]Department of Earth and Space Science, Graduate School of Science, Osaka University, Toyonaka, Osaka 560-0043, Japan
[2]Department of Earth and Planetary Science, Graduate School of Science, University of Tokyo, Hongo, Tokyo 113-0033, Japan

(*Received April* 25, 2001; *accepted in revised form September* 5, 2001)

Abstract—Variations in bulk Mg/Si ratios in the various groups of chondritic meteorites indicate that Mg/Si fractionation occurred in the primitive solar nebula. Enstatite ($MgSiO_3$) evaporates incongruently forming forsterite (Mg_2SiO_4) as an evaporation residue; therefore, evaporation of enstatite produces Mg/Si variations in solid (Mg-rich) and gas (Si-rich) and must be considered as a probable process responsible for Mg/Si fractionation recorded in chondrites. To understand the evaporation kinetics of enstatite, incongruent evaporation experiments on enstatite single crystals have been carried out in vacuum and in hydrogen gas at temperatures of 1300 to 1500°C. A polycrystalline forsterite layer is formed on the surface of enstatite by preferential evaporation of the SiO_2 component, both in vacuum and in hydrogen gas. The thickness of the forsterite layer in vacuum increases with time in the early stage of evaporation and later the thickness of the forsterite layer remains constant (several microns). This is due to the change in the rate limiting process from surface reaction plus nucleation and growth to diffusion in the surface forsterite layer. The activation energy of the diffusion-controlled evaporation rate constant of enstatite is 457 (±58) kJ/mol. A thinner forsterite layer is formed on the surface of enstatite in hydrogen gas than in vacuum. Evaporation of enstatite in hydrogen gas is also considered to be controlled by diffusion of ions through the forsterite layer. The thin forsterite layer formed in hydrogen gas is ascribed to the enhanced evaporation rate of forsterite in the presence of hydrogen gas.

The results are applied to incongruent evaporation under the solar nebular conditions. The steady thickness of the forsterite of nebular pressure–temperature conditions is estimated to be submicron because of the enhanced evaporation rate of forsterite under hydrogen-rich nebular conditions if evaporated gases are taken away immediately and no back reaction occurs (an open system). Because enstatite grains in the solar nebula would be comparable to the estimated steady thickness of forsterite, evaporation of such enstatite grains under kinetic conditions could play an important role in producing variations in Mg/Si ratios between solid and gas in the solar nebula. *Copyright © 2002 Elsevier Science Ltd*

1. INTRODUCTION

Chondrites are primitive meteorites that record the evolution of the early solar system. Their elemental abundance patterns are more or less fractionated from solar abundances except for CI chondrites (e.g., Dodd, 1981; Kallemeyn, 1988; Sears and Dodd, 1988; Wasson and Kallemeyn, 1988), implying that elemental fractionation processes occurred in the primitive solar nebula before aggregation of dust and accumulation of chondrite parent bodies. Many researchers have tried to reveal the chemical evolution of the solar nebula (e.g., Larimer and Anders, 1967, 1970; Wasson and Chou, 1974; Wai and Wasson, 1977; Kerridge, 1979; Larimer, 1979; Sears and Weeks, 1986; Sears et al., 1996). The calculated equilibrium condensation sequence, in which gas–solid equilibria are assumed, has been used in many articles as a framework for the discussion of chemical fractionations in the solar nebula (e.g., Larimer and Anders, 1967, 1970; Grossman, 1972; Lewis, 1972; Kerridge, 1979; Larimer, 1979; Wood and Hashimoto, 1993; Petaev and Wood, 1998).

However, disequilibrium could be important for elemental fractionations if the timescale of equilibration is longer than the evolutional timescale of the system. The fundamental processes that are responsible for elemental variations among different phases in the solar nebula are condensation of gas and evaporation of condensed phases. Understanding the kinetics of those processes allows us to compare the timescale of chemical reactions with the evolutional timescale of the solar nebula and to evaluate the disequilibrium of reactions in the solar nebula. A good example for demonstrating the importance of disequilibrium is the CO to CH_4 conversion, which is predicted to proceed at 500 to 700 K in the nebula in equilibrium models. Lewis and Prinn (1980), however, showed that the conversion would not have been completed within the timescale of nebular evolution because of its slow kinetics.

Magnesium and Si are the two most abundant lithophile elements in the solar system (e.g., Anders and Grevesse, 1989). The bulk elemental data of chondrites show that there are variations in Mg/Si ratios in the various groups of chondrites (e.g., Dodd, 1981; Wasson and Kallemeyn, 1988; Lodders and Fegley, 1999). All the authors suggest that Mg/Si fractionation processes occurred in the solar nebula. The Mg/Si (atomic) ratios of carbonaceous chondrites (CI, CM, CO, CV, CK, and CR) are within the range of 1.045 to 1.075 (Dodd, 1981; Wasson and Kallemeyn, 1988; Lodders and Fegley, 1999) and similar to the solar ratio (1.074; Anders and Grevesse, 1989). The exception is CH chondrites, which have a Mg/Si ratio of

* Author to whom correspondence should be addressed, at Department of Geological Sciences, Arizona State University, Tempe, AZ 85187-1404, USA (tachi@asu.edu).

0.967 (Lodders and Fegley, 1999). Kakangari-type chondrites have a Mg/Si ratio (1.053; Lodders and Fegley, 1999) that is similar to the solar ratio. The Mg/Si ratios of ordinary chondrites and enstatite chondrites, 0.926 to 0.957 and 0.730 to 0.876 (Dodd, 1981; Wasson and Kallemeyn, 1988; Lodders and Fegley, 1999), respectively, are ~0.9 and 0.8 to 0.7 times below the solar ratio. R chondrites also have a Mg/Si ratio (0.828) below the solar ratio (Lodders and Fegley, 1999). This variation in Mg/Si ratios in the various groups of chondrites implies that Mg/Si fractionation of the parent materials of chondrites either experienced Mg depletion or Si enrichment in the different chondrite-forming regions.

There are several models for the Mg/Si fractionation. Kerridge (1979) and Larimer (1979) explained Mg/Si variations among chondrites by subtraction of refractory components, which consisted of forsterite and calcium-aluminum-rich inclusions (CAI)-like objects, from the CI composition before formation of enstatite based on the equilibrium condensation model, in which enstatite was formed by the reaction of gaseous Si with forsterite. Petaev and Wood (1998) developed an equilibrium condensation with partial isolation model, in which a specific fraction (ξ) of condensates was removed from the reactive system as condensation proceeded. They proposed that the chemistry of carbonaceous and enstatite chondrites would be explained by condensation with partial isolation with ξ of $\leq$0.1 and 0.7 to 1.5%, respectively. Krot et al. (2000) have explained the Mg/Si ratio and the reducing formation condition of enstatite chondrites as a result of the addition of presolar SiC grains in their formation region. Evaporation of silicate melts also produces Mg/Si variations between gas and melt because the SiO_2-rich component evaporates faster than the MgO-rich component (e.g., Hashimoto, 1983; Nagahara and Ozawa, 1996a; Cohen et al., 2000; Wang et al., 2001). Sears et al. (1996) calculated evaporation losses of Si and Fe during chondrule formation on the basis of experimental data of Hashimoto (1983). They concluded that volatile-poor reduced chondrules (type I) would have been formed by evaporation and reduction of volatile-rich ferroan chondrules (type II), whereas Grossman (1996) mentioned that the chemistry of chondrules should not have been affected by evaporation during their formation but by chemical differences among precursors.

The focus of this article is evaporation kinetics of enstatite ($MgSiO_3$). Evaporation experiments of enstatite under kinetic conditions were performed to characterize Mg/Si fractionation in the solar nebula for the following reasons. First, equilibrium calculations show that enstatite evaporates incongruently to form forsterite as evaporation residue. Evaporation of enstatite thus produces Mg/Si variations between solid (Mg-rich) and gas (Si-rich) and may be an important process for Mg/Si fractionation. Second, there are no experimental studies of evaporation kinetics of enstatite, although incongruent evaporation of enstatite has been confirmed in equilibrium evaporation experiments in a Knudsen cell (Kushiro and Mysen, 1991). Third, enstatite is the magnesium end member of low-Ca pyroxene, which is one of the major minerals in primitive materials such as chondrules, matrixes of O-, E- and less altered C-chondrites (Brealey and Jones, 1998, and references therein) and interplanetary dust particles (Rietmeijer, 1998, and references therein). Also, the short-wavelength spectrometer observation by the Infrared Space Observatory shows direct evidence of the presence of Mg-rich pyroxene in comets, circumstellar envelopes around young stars, evolved stars, and planetary nebulae (e.g., Waelkens et al., 1996; Waters et al., 1996; Jäger et al., 1998). Accordingly, enstatite would have existed in the early solar nebula as a major Mg-, Si-bearing phase. Furthermore, the Mg/Si ratio of enstatite (=1) is almost the same as the solar Mg/Si ratio, so enstatite is approximately regarded as a host mineral of Mg and Si in the system with solar abundances if all iron is present as metal.

If evaporation of enstatite contributes significantly to Mg/Si variations in solid and gas in the solar nebula, chondrites that are enriched in Si (or depleted in Mg) relative to the solar abundance could have formed by condensation of a gas enriched in Si by incongruent evaporation of enstatite. This scenario could have occurred in an active turbulent solar nebula. Because dust particles, which accumulate and grow in the nebula, tend to have a faster inward drift velocity to the Sun than gas and fine dust particles due to gas drag, solid–gas separation is not unlikely. If solid–gas separation occurred in the temperature range of enstatite evaporation, Mg-rich solid residues would be removed from the system, and the remaining gas would be enriched in Si.

Here we report the results of our evaporation experiments of enstatite, which were carried out in vacuum and in hydrogen gas. We apply the experimental evaporation rates to the evaporation behavior of enstatite grains under solar nebula conditions in an open system, where gas evaporating from dust grains leaves the system and no back reaction occurs, to study Mg/Si fractionation with time. The evaporation behavior of enstatite grains in the presence of ambient evaporated gas, which should also be discussed because evaporation in the solar nebula would not necessarily occur in a fully open system, will be presented elsewhere (Tachibana et al., in preparation).

2. EXPERIMENTS

2.1. Synthesis of Orthoenstatite Crystals

Single crystals of orthoenstatite were synthesized by the flux method (Ozima, 1982) and then used as starting materials. Nutriment of MgO and SiO_2 of >99% purity, mixed with enstatite stoichiometry, was added to the flux of Li_2CO_3, MoO_3, and V_2O_5 of 99.99% purity that was mixed in the proportions of 34.3, 55.9, and 9.8 wt%, respectively. The weight ratio of the nutriment to the flux was 0.05. The mixture of nutriment and flux was heated in a platinum crucible at 950°C for 100 h in the air, then cooled to 700°C at an average cooling rate of 0.5°C/h and to room temperature at ~50°C/h. Synthesized orthoenstatite crystals were separated from the solvent by washing in hot water. A few tens of orthoenstatite single crystals with typical sizes of 1 × 2 × 3 mm were obtained usually in a single run. X-ray powder diffraction (XRD) patterns of some crystals were obtained by the Rigaku powder diffractometer with Cu-K_α radiation, installed at the Department of Earth and Space Science, Osaka University, and they were confirmed to be orthoenstatite.

The crystals were transparent and elongated to the c-axis, and the {010}, {210}, and {100} faces were well developed perpendicular to the c-axis. In particular, the {010} face was the most developed face, and platy crystals with wide {010}

Table 1. Composition of synthesized orthoenstatite crystals (20 analyses).[a]

Element	Average (wt%)	Max (wt%)	Min (wt%)	cf. $MgSiO_3$
MgO	39.83	40.44	38.89	40.15
SiO_2	60.04	61.26	58.77	59.85
V_2O_5	0.12	0.34	0.01	0
MoO_3	ND	ND	ND	0
Li_2O	—	—	—	0
Total	99.99	101.26	98.01	100

[a] Max, maximum; Min, minimum.

faces were sometimes observed. The {111} and {211} faces were also developed.

Synthesized crystals were stoichiometric enstatite and contained a small amount of V_2O_5 as an impurity (~0.12 wt%) (Table 1). Molybdenum was not detected by the electron microprobe analyses (JEOL 733). Although the lithium content was not measured, Ito (1975) reported that orthoenstatite crystals, which were synthesized in the Li_2O-MoO_3-V_2O_5 flux as in this experiment, contained Li_2O = 0.17 wt% and V_2O_5 = 0.27 wt% as major impurities. Our synthesized crystals probably contain similar amounts of Li_2O as impurities.

2.2. Evaporation Experiments of Enstatite in Vacuum and Hydrogen Gas

Experiments were conducted both in vacuum and in hydrogen gas. Two vacuum furnaces, furnace 1 and furnace 2, described by Ozawa and Nagahara (2000) and Tsuchiyama et al. (1998), respectively, were used. Furnace 1 had a tungsten mesh heater (5 cm in diameter and 10 cm in height), which was set in a vacuum chamber connected to a turbo molecular pump. The temperature was measured and controlled within ±1°C by a W_5Re_{95}-$W_{26}Re_{74}$ thermocouple located ~5 mm above the sample. The thermocouple was calibrated against melting temperatures of Ni (1455°C) and Co (1494°C). Furnace 1 was used for experiments in vacuum because it could reach higher vacuum ($\leq 10^{-10}$ bar at room temperature) than with furnace 2 ($\sim 10^{-9}$ bar at room temperature). The pressure in the vacuum chamber was measured by an ionization gauge that was attached to the chamber. Furnace 2 consisted of two vacuum chambers (a sample chamber and a heater chamber) that were evacuated separately by diffusion pumps. Two separate vacuum chambers were used to prevent the sample chamber from being contaminated with gases evaporated from the tantalum heater. The tantalum heater was set in the heater chamber and surrounded a molybdenum crucible (1.6 cm in diameter and 12.4 cm in height) in the sample chamber (see fig. 1 in Tsuchiyama et al. 1998). The temperature of the sample was measured by a $W_{95}Re_5$-$W_{74}Re_{26}$ thermocouple located directly at the side of the sample. The experimental temperature was controlled within ±5°C by another thermocouple located in the heater chamber and beneath the molybdenum crucible. Melting temperatures of Au (1064.43°C), Ni (1455°C), and Pd (1554°C) were used to calibrate the thermocouple. Furnace 2 was used in experiments in hydrogen gas because hydrogen gas could be flowed through the sample chamber. An ionization gauge, which was attached to the sample chamber, was used to measure the hydrogen pressure by taking the ionization coefficient of H_2 into account.

In the vacuum experiments, a single crystal of enstatite was put on a molybdenum-mesh sheet and placed in the hot spot of the furnace. The wide surfaces of the crystal were polished with silicon carbide abrasives (no. 3000) to remove the small amount of residual flux materials left on the surface. After the pressure in the vacuum chamber reached less than $\sim 5 \times 10^{-9}$ bar, it was preheated to 500°C for 0.5 to 5 h to evacuate gases that were released from the vacuum chamber. Then it was heated to an experimental temperature at ~20°C/min. The sample was heated for the desired duration (2 to 240 h) at the experimental temperature (1300 to 1500°C) with continuous evacuation. The sample was quenched by shutting off the power supply. It took a few minutes to cool down below 1000°C and about an hour to cool to room temperature. The pressure in the furnace during an experiment was $\sim 10^{-9}$ bar. The estimated mean free path of SiO, which is the dominant Si-bearing gas species for evaporation of forsterite (Nichols et al., 1998), is about 100 m and much longer than the specific length of the furnace, suggesting that Langmuir evaporation occurs (i.e., no back-reaction takes place).

The surface of the sample after each experiment was investigated with a scanning electron microscope (SEM) equipped with an electron microprobe analyzer (JEOL 733, installed at Department of Earth and Space Science, Osaka University, and JEOL 840, installed at Department of Earth and Planetary Sciences, University of Tokyo). The surface chemical composition was also analyzed by EPMA with a focused beam at an accelerating voltage of 15 kV and a beam current of 12 nA on the Faraday cup. The sample was mounted in methyl methacryltate monomer, which had a low viscosity and permeated easily, even into small cracks of samples, before solidification. The sample was cut perpendicular to the c-axis of enstatite to make a thin section. The thickness of the residual layer on the crystallographic faces of enstatite ({010}, {210}, and {100}) was measured under an optical microscope with 10 to 134 measurements for each sample. Only a part of the layer could be measured for samples that were broken during experiments or sample preparation after heating. The thickness that was measured for a part of the layer of broken samples was regarded as that of the whole layer because differences in the thickness of the layer on different crystallographic faces of enstatite were not detected.

In the experiments in hydrogen gas, a prism-shaped enstatite crystal was prepared by cutting off both the pyramids on the sides perpendicular to the c-axis. The surfaces of the crystal were polished with silicon carbide abrasives (no. 3000) as noted above in the vacuum experiments. The surface area of an enstatite prism (S) was measured by image analyses, assuming a perfect prism with flat surfaces. The uncertainty of the measurement of the surface area was estimated to be ~30%. The sample was put in a box made of molybdenum foil and set in a hot spot of the molybdenum crucible. Hydrogen gas was flowed into the sample chamber after the pressure in the chamber reached $\sim 5 \times 10^{-9}$ bar. The hydrogen pressure in the chamber was kept constant (7.2×10^{-7}, 2.0×10^{-6}, or 6.1×10^{-6} bar) by adjusting the flow rate of hydrogen gas by a microvalve during experiments under continuous evacuation. The sample was preheated at ~500°C for a few hours and then

heated to the desired temperature. It took ~15 min to heat the sample from 500°C to the experimental temperature. Experimental temperatures were 1300, 1400, and 1500°C, and heating duration ranged from 1 to 44 h. After heating, samples were quenched by shutting off the power supply. It took a few minutes to cool down below 1000°C. The weight change of the sample (ΔW) was measured by an electronic microbalance with a precision of ± 0.1 mg. The weight change of the molybdenum box in each experiment was within the precision of the balance. The surface of the sample was checked with SEM, and its chemical composition was analyzed by EPMA with an accelerating voltage of 5 kV and a spot beam current of 5 nA on the Faraday cup.

To identify minerals in the very thin layer of evaporation residues, 10 to 15 enstatite crystals were put together in a molybdenum box and heated in vacuum or in hydrogen gas in the furnace 2. Heated samples were powdered in an agate mortar, and their XRD patterns were obtained. Infrared (IR) spectra of some powdered samples were also obtained by the Jasco FT/IR-350 spectrometer installed at Kyoto Pharmaceutical University.

3. RESULTS

3.1. Experiments in Vacuum

3.1.1. Samples and Evaporation Residue

Samples after experiments were very fragile because protoenstatite, which was transformed from orthoenstatite at experimental temperatures, converted into brittle, polysynthetically twinned clinoenstatite by rapid cooling (Smith, 1975). Some samples broke into pieces, and some pieces fell from the molybdenum mesh. The original surfaces of the enstatite samples were covered with an evaporation residue, but the newly formed broken surfaces were not, implying that samples did not break during heating at the experimental temperature but during cooling by the proto-clino inversion. A precise measurement of weight change of a sample by evaporation was difficult because of the loss of some broken pieces of the sample; therefore, the weight change was not used to evaluate the evaporation rates in vacuum. Instead, the thickness of the residual forsterite layer was used to estimate evaporation rates.

The samples turned a bluish color after heating; this was most conspicuous in the pyramidal sectors of samples. The bluish color is probably due to change of the oxidation state of vanadium (probably reduction), which was incorporated into samples as an impurity during the crystal growth (Table 1), by heating under reducing vacuum conditions. The difference of bluish color in a sample may be ascribed to differences in the concentrations of vanadium in different growth sectors. Because the concentration of vanadium in the sample is quite low (Table 1), the change in color does not seem to affect results in this study. It is unlikely that recondensation (back-reaction) of evaporated gases make the bluish color because no back-reaction occurs in these experiments, as mentioned above. Furthermore, recondensation would produce a uniform color on all surfaces.

Figures 1a–d show SEM images of the surface of heated samples. The sample surfaces were very rough and seemed to be covered with tiny crystal-like objects (Figs. 1a–c). The chemical composition of the surface materials analyzed with EPMA showed that the surface of all samples heated at 1400 to 1500°C had forsterite stoichiometry, although precise quantitative analyses were difficult because of the roughness of the surface.

Thin sections viewed with an optical microscope showed that the evaporation residue is a polycrystalline layer consisting of individual crystals that grew to several tens of microns (Fig. 1e). The thickness of the residual layer was several microns, and the layer was too thin to be identified by microprobe analysis. Polysynthetic twinning of the host enstatite crystal was also observed.

An XRD pattern of the sample heated at 1500°C for 94 h in vacuum showed the diffraction pattern of forsterite in addition to that of clinoenstatite (Fig. 2a). An IR spectrum of the same sample shows an absorption feature at ~610 cm^{-1}, which is a distinct feature distinguishing forsterite from pyroxene. The sample also has a clear absorption feature at 405 cm^{-1}, which suggests the presence of orthoenstatite. Smith (1975) reported that the protoclino inversion of enstatite was accomplished by quenching within a second or less, whereas slower cooling through the range of 700 to 600°C produced crystals that contained as much as 50% of orthoenstatite. The samples in these experiments might be partly inverted from protoenstatite to orthoenstatite because the cooling rate in our experiments was much slower than quenching.

The chemical composition, optical microscopic observation, XRD patterns, and IR spectra clearly show the presence of crystalline forsterite as an evaporation residue. Hence, the formation of forsterite by incongruent evaporation of enstatite was confirmed under kinetic conditions as well as at near-equilibrium condition in the Knudsen cell (Kushiro and Mysen, 1991).

Step-like textures were observed on the surface of evaporation residue formed at 1500°C (Fig. 1a). Similar textures have been reported in evaporation experiments on forsterite (Nagahara and Ozawa, 1999) and referred to as evaporation steps, which are the surface textures formed by evaporation (Hirth and Pound, 1963). The step-like texture in this study suggests that residual forsterite also evaporated during the experiment.

Experiments with a short heating duration showed that residual forsterite crystals (several microns in thickness) were formed sporadically on the surface of enstatite in the initial stage of evaporation (Fig. 1d), with a tendency to cover the whole surface as evaporation proceeds. It took ~10 to 20 h and ~5 h for evaporation residues to cover the whole surface at 1400 and 1500°C, respectively (Table 2), whereas only a small amount of evaporation residue with the forsterite stoichiometry was found on the surface, even for the sample heated at 1300°C for 120 h.

3.1.2. Thickness of Residual Forsterite Layer

The thickness of the residual forsterite layer, X_{Fo}, on the crystallographic faces of enstatite ({010}, {210}, and {100}) was measured under an optical microscope. The average thickness was listed with maximum and minimum values of measured thickness and number of analyses in Table 2 and plotted against heating duration in Figure 3. The uncertainty of the thickness is shown at the 99% confidence level, which was

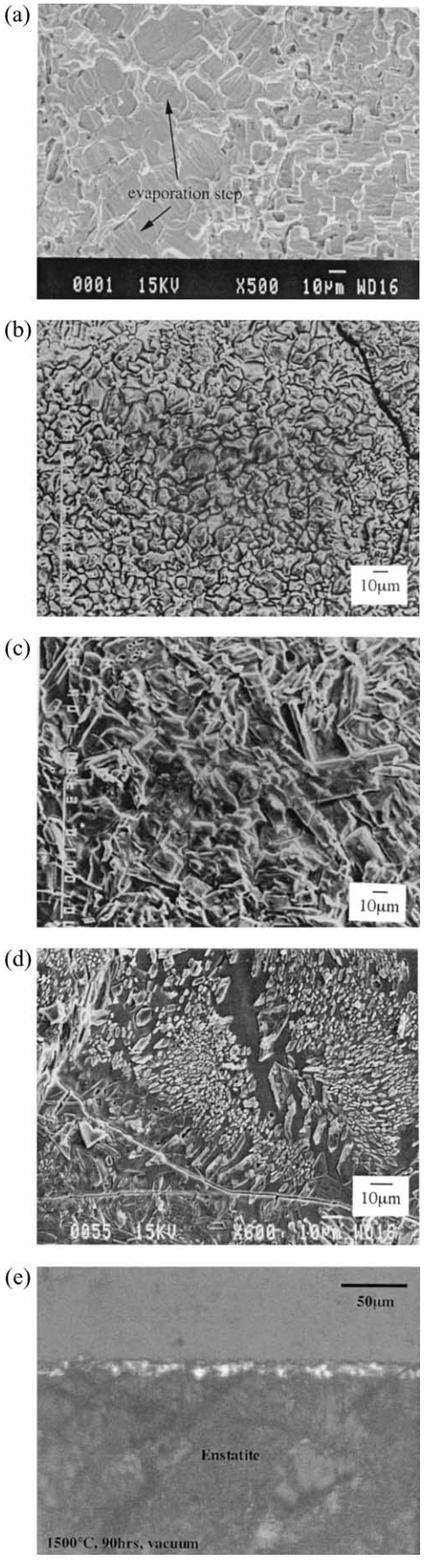

Fig. 1. SEM photomicrographs (secondary electron image) of the surfaces of samples heated in vacuum (a–d) and an optical photomicrograph (transmitted cross-polarized light) of a thin section of a sample (e). (a) 1500°C, 22 h. The whole surface is covered with forsterite crystals. A step-like texture is found on the surface (arrow). This texture resembles that found in evaporation experiments on forsterite in vacuum (Nagahara and Ozawa, 1999). (b) 1450°C, 55 h. The whole surface is covered with forsterite crystals. (c) 1400°C, 194 h. The whole surface is covered with forsterite crystals. (d) 1400°C, 10 h. Tiny residual forsterite crystals (bright) were randomly formed on the surface of enstatite (dark). (e) A cross section of the sample heated at 1500°C for 90 h in vacuum, the {010} face is seen in the photograph. It can be seen that the evaporation residue is a polycrystalline layer. The size of each residual crystal is between several and several tens of microns.

obtained by multiplying a mean error by a 99% confidential factor of the *t* distribution.

Increases of X_{Fo} with heating duration up to several tens of hours were found at all temperatures studied. The thickness of the forsterite layer becomes constant at 1400°C (~6 μm) after heating for ~90 h (Fig. 3a), whereas it decreases to a constant

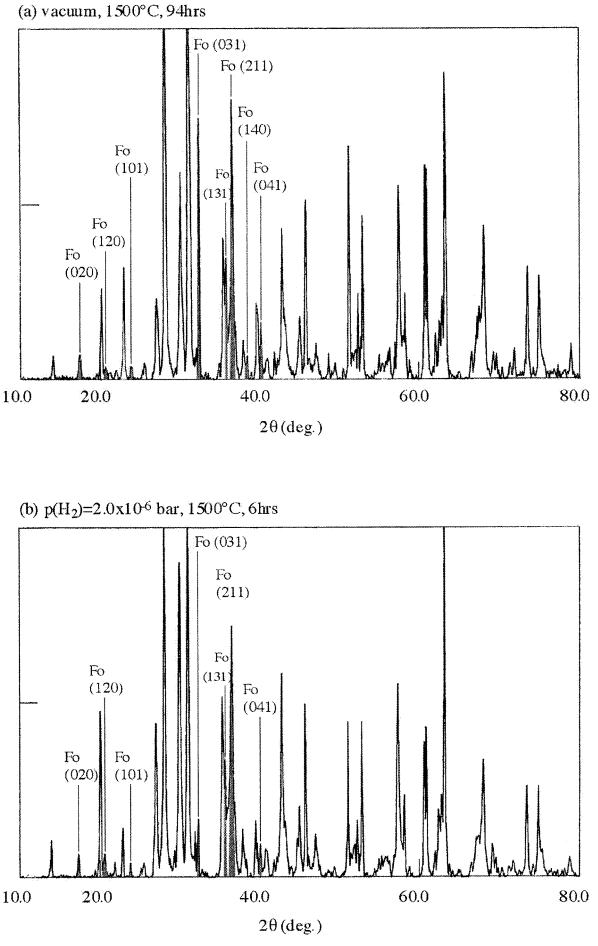

Fig. 2. XRD patterns of samples heated in vacuum and hydrogen gas. The diffraction pattern of forsterite (labeled and shown in gray) is seen in addition to that of clinoenstatite, which was transformed from protoenstatite during rapid cooling. (a) Vacuum at 1500°C for 94 h. (b) $p(H_2) = 2.0 \times 10^{-6}$ bar at 1500°C for 6 h.

Table 2. Experimental conditions in vacuum and the thickness of the residual forsterite layer (X_{Fo}).[a]

T (°C)	Time (hr)	X_{Fo} (μm)	Max X_{Fo} (μm)	Min X_{Fo} (μm)	No. analyses	99% confidence interval (μm)
1500	5	(almost covered)	—	—	—	—
1500	14	3.78	6.44	2.15	71	0.286
1500	22	3.90	9.42	1.63	48	0.793
1500	30	5.20	11.33	2.34	35	1.000
1500	60	6.14	7.08	5.14	11	0.604
1500	90	7.39	15.23	3.12	37	1.250
1500	110	5.96	8.19	2.85	27	
1500	135	3.47	4.51	2.36	12	0.753
1500	150	3.91	8.96	1.60	43	0.699
1500	180	3.60	6.25	1.74	50	0.431
1450	30	5.25	7.22	2.71	28	0.520
1450	40	5.98	8.33	3.89	22	0.770
1450	55	7.25	13.89	2.78	35	1.430
1450	110	7.34	11.46	4.10	38	0.846
1450	150	7.12	12.36	4.44	64	0.628
1450	180	5.92	8.89	3.13	44	0.462
1450	240	5.71	12.08	3.26	44	0.647
1400	2	(sporadic)	—	—	—	—
1400	5	(sporadic)	—	—	—	—
1400	10	(partially covered)	—	—	—	—
1400	22	2.84	3.40	2.29	10	0.555
1400	35	3.25	4.19	2.08	57	0.151
1400	45	4.55	6.01	2.47	42	0.301
1400	70	5.28	6.51	3.87	134	0.146
1400	90	6.54	9.58	4.51	121	0.229
1400	120	6.43	8.33	4.03	85	0.288
1400	150	6.42	8.82	4.44	26	0.581
1400	194	6.70	8.75	5.00	85	0.271
1300	120	(sporadic)	—	—	—	—

[a] X_{Fo} was measured under an optical microscope.

thickness at 1450°C (~5.5 μm) (Fig. 3b) and 1500°C (~4 μm) (Fig. 3c) after heating of ~70 h and ~90 h, respectively. Drastic depletion of X_{Fo} is observed at 1500°C.

Our results indicate that there seem to be at least two different evaporation modes of enstatite: a mode in which X_{Fo} increases with time observed in the early stage of evaporation, and another in which X_{Fo} becomes constant in the later stage.

3.2. Evaporation in Hydrogen Gas

Samples heated in hydrogen gas were fragile and bluish in color, which were caused by the proto-clino inversion during cooling and the change of the oxidation state of vanadium in the sample, respectively. These effects were also observed in samples heated in vacuum. The mean free path of SiO in hydrogen gas of 7×10^{-7} to 6×10^{-6} bar at experimental temperatures (1300 to 1500°C) is above ~1 m, and thus, little back-reaction occurs. The color of the surface attached to the molybdenum box was slightly black and had a different appearance from other surfaces.

Evaporation step and tiny crystals found in the vacuum experiments were not observed in the hydrogen gas experiments (Fig. 4). Furthermore, no forsterite layer was observed in cross sections of the samples under an optical microscope. Microprobe analyses of the surfaces at an accelerating voltage of 15 kV and a spot beam current of 12 nA on the Faraday cup indicated a Mg/Si ratio at the surface between 1 (=enstatite) and 2 (=forsterite). However, the microprobe analyses at an accelerating voltage of 5 kV and a spot beam current of 5 nA on the Faraday cup, by which the characteristic X-rays were generated from a shallower region near the surface than the analyses at 15 kV and 12 nA, showed that the surface composition had forsterite stoichiometry. XRD patterns (Fig. 2b) and an IR absorption feature around 610 cm^{-1} also suggested the existence of forsterite. Hence, we conclude that enstatite evaporates incongruently to form a very thin layer of forsterite in hydrogen gas as well as in vacuum, but that the layer in hydrogen gas is much thinner than that in vacuum. The layer is presumably submicron in thickness, which is too thin for an accurate determination with an optical microscopic observation.

The weight change of the sample (ΔW) was thus used to estimate evaporation rates instead of the thickness of the forsterite layer (Table 3). The sample was put in a molybdenum box instead of the mesh used in the vacuum experiments for precise measurements of weight. The weight changes of the samples per unit area ($\Delta W/S$) are shown in Figure 5. Because the surface of enstatite attached to the molybdenum box seemed to be different from other surfaces, the attached surface area was excluded from the estimation of the total surface area (S). Although the change of the total surface area (S) should be considered because S becomes smaller as evaporation proceeds, it is not considered because it would be within the uncertainties of the measurements of the initial S as long as the evaporation fraction was small (<25%). Enstatite appears to lose its mass linearly with time, and the evaporation rate is larger at higher hydrogen pressures and higher temperatures (Fig. 5).

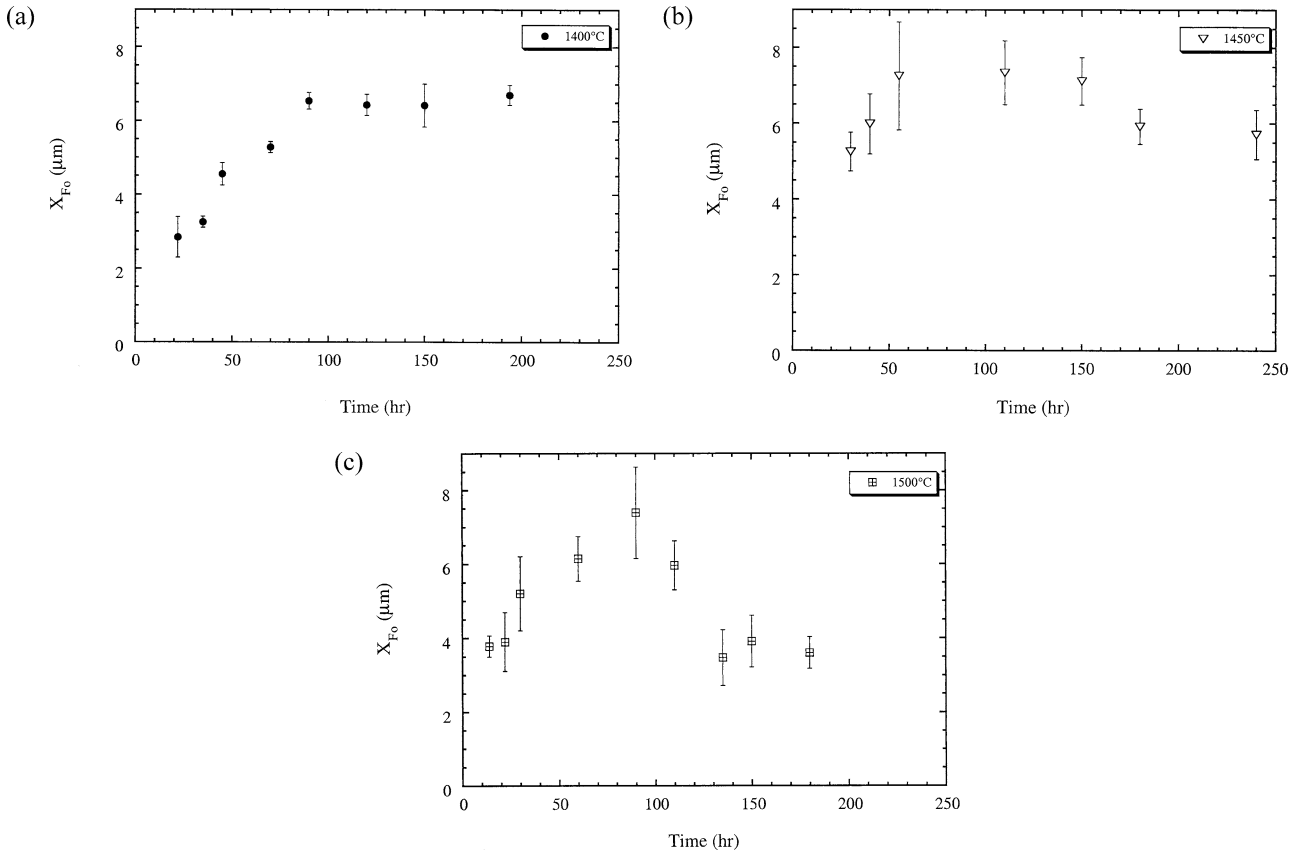

Fig. 3. Change of the thickness of the residual forsterite layer, X_{Fo}, with heating duration in vacuum experiments at different temperatures. (a) 1400°C. X_{Fo} increases with time and then becomes constant. (b) 1450°C. X_{Fo} increases with time, then decreases and approaches a constant thickness. (c) 1500°C. X_{Fo} increases with time, then decreases and approaches a constant thickness, as does X_{Fo} at 1450°C. The depletion of X_{Fo} is more abrupt than at 1450°C. Errors show the 99% confidence levels, which are obtained by multiplying a mean error by a 99% confidence factor of the *t* distribution.

4. DISCUSSION

4.1. Evaporation Kinetics of Enstatite in Vacuum

4.1.1. Possible Origins of the Forsterite Layer and Its Evaporation

Forsterite on the surface of enstatite can be formed by a back-reaction (recondensation) of evaporated gas at the surface of enstatite or by transition of enstatite to forsterite as a result of preferential loss of Si and O from the surface. The first case is unlikely because the mean free path of gas species at the experimental conditions is much longer than the size of furnace and very little condensation occurs, as mentioned above. Thus, we conclude that forsterite is formed as an evaporation residue by incongruent evaporation of enstatite.

A step-like texture of the residual forsterite layer formed at 1500°C (Fig. 1a) is similar to the surface texture of forsterite, which evaporated at 1500°C in vacuum (Nagahara and Ozawa, 1999). The evaporation rate of forsterite at 1500°C in vacuum is 0.27 μm/h along the c-axis (Nagahara and Ozawa, 1999), i.e., forsterite of $\sim$30 μm thickness evaporates within 100 h at 1500°C. The surface texture and the evaporation rates in previous experiments suggest that evaporation of forsterite also occurs simultaneously with evaporation of enstatite (formation of forsterite). It is thus important to consider evaporation of forsterite when discussing the evaporation mechanism of enstatite.

4.1.2. Diffusion-Controlled Evaporation

Incongruent evaporation of enstatite is the result of several processes: reaction at the forsterite–enstatite interface, transport through the forsterite layer, and reaction at the surface of forsterite. The slowest process is the rate-limiting process. As shown below, our results for longer heating duration are explained by diffusion-controlled transport through the forsterite layer as a rate-limiting process. Thus, reactions at the forsterite–enstatite interface and at the surface of forsterite do not control the overall reaction kinetics.

When a residual forsterite layer on enstatite is compact, the rate-limiting process for evaporation of enstatite should be diffusion of ions through the compact forsterite layer. The diffusion flux through the forsterite layer (J_{diff}) is expressed by

$$J_{diff} = -D\frac{dC}{dX_{Fo}}, \quad (1)$$

where D is the diffusion constant and dC/dX_{Fo} is the compo-

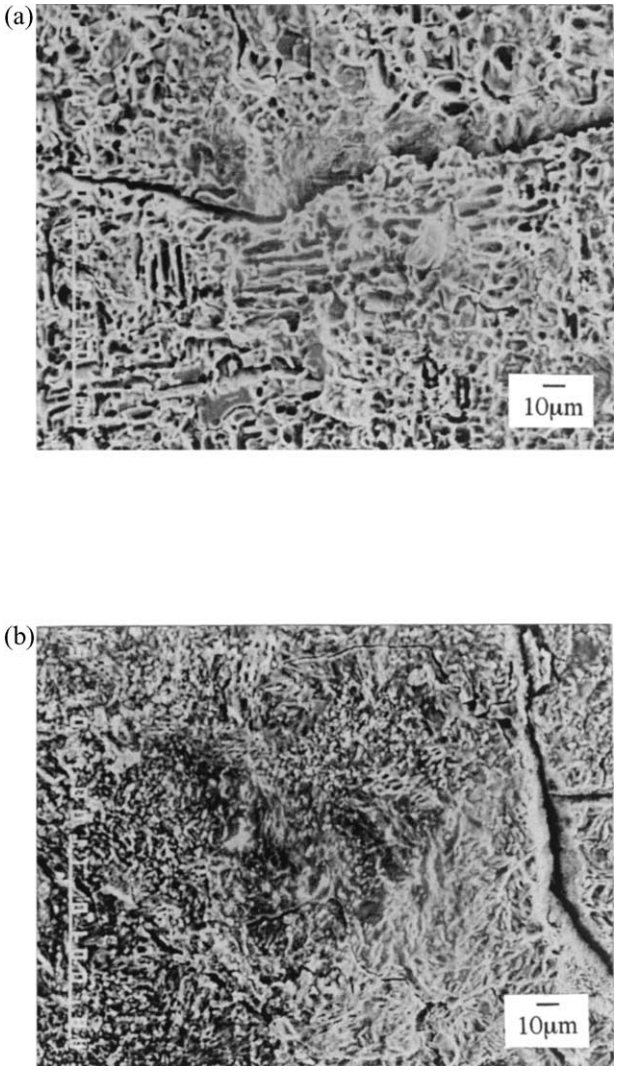

Fig. 4. SEM photomicrographs of samples heated in hydrogen gas. The surface is rough, and textures are slightly different from those in vacuum. (a) $p(H_2) = 2.0 \times 10^{-6}$ bar at 1500°C for 4 h. (b) $p(H_2) = 2.0 \times 10^{-6}$ bar at 1400°C for 3 h.

sitional gradient in the forsterite layer. If the enstatite–forsterite and forsterite–gas interfaces are in equilibrium, the compositional difference between the interfaces, which is determined by equilibria at the interfaces, should be constant. Thus, dC/dX_{Fo} can be written as $\Delta C/X_{Fo}$, where ΔC is the compositional difference between the interfaces. The diffusion flux is converted to the thickening rate of the forsterite layer (dX_{Fo}/dt) as follows:

$$\frac{dX_{Fo}}{dt} = \nu_{Fo} J_{diff} = -\nu_{Fo} D \frac{\Delta C}{X_{Fo}} = \frac{\kappa_{En}}{2X_{Fo}}, \quad (2)$$

$$\kappa_{En} \equiv 2\nu_{Fo}\, D(-\Delta C), \quad (3)$$

where v_{Fo} is the molar volume of forsterite and κ_{En} ($L^2\ t^{-1}$) is the diffusion-controlled evaporation constant of enstatite. Eqn. 2 is usually used in oxidation of metals to express the thickening rate of the oxidized layer and shows that X_{Fo} is proportional to $t^{1/2}$.

Because in this case forsterite also evaporates, a corresponding law should be included in Eqn. 2, as mentioned above:

$$\frac{dX_{Fo}}{dt} = \frac{\kappa_{En}}{2\,X_{Fo}} - k_{Fo}, \quad (4)$$

where k_{Fo} is the surface-reaction controlled evaporation rate constant of forsterite ($L\ t^{-1}$). The same equation is used to explain the oxidation kinetics of chromium, which was expressed by diffusion-controlled oxidation of Cr and evaporation of volatile Cr_2O_3 (Tedmon, 1966).

When X_{Fo} is small, the formation rate of the forsterite layer ($\kappa_{En}/2X_{Fo}$) is much larger than k_{Fo}, and X_{Fo} increases. The formation rate of forsterite decreases as X_{Fo} increases. When X_{Fo} achieves the thickness expressed by

$$X^*_{Fo} = \frac{\kappa_{En}}{2k_{Fo}}, \quad (5)$$

the net formation rate of forsterite becomes zero ($dX_{Fo}/dt = 0$), and evaporation of enstatite reaches a steady state where the formation and evaporation of forsterite are balanced. Further evaporation proceeds with the constant thickness of the forsterite layer (X^*_{Fo}) at the evaporation rate of forsterite (k_{Fo}) until enstatite is totally converted to forsterite.

The thickness of the forsterite layer, X_{Fo}, in our experiments seems to be constant for samples heated longer than 135 h at 1500°C, 180 h at 1450°C, and 90 h at 1400°C, respectively (Fig. 3), which can be attributed to X^*_{Fo} in Eqn. 5. We obtained κ_{En} from Eqn. 5 by using constant thickness in experiments and k_{Fo} extrapolated from data in Hashimoto (1990) (Table 4). In the temperature range of 1400 to 1500°C, κ_{En} shows an Arrhenius relation within experimental uncertainties (Fig. 6):

$$\ln \kappa_{En}(cm^2\ s^{-1}) = 5.26(\pm 4.05) - \frac{457(\pm 58)(kJ/mole)}{RT}. \quad (6)$$

It should be noted that the compositional gradient (ΔC) in the forsterite layer, which is included in κ_{En}, may depend on the partial pressure of oxygen in the surrounding gas atmosphere. Thus, one should be careful when applying the obtained κ_{En} in vacuum to other conditions.

Imae et al. (1993) found that enstatite was formed on the surface of forsterite by the diffusion-controlled reaction of forsterite with a Si-rich gas. They proposed four diffusion models and recommended one model because the volume change of formation of enstatite at the forsterite–enstatite interface was smallest and the strain due to the volume change appeared be minimal. Four different models of diffusion processes are possible for evaporation of enstatite and formation of forsterite to satisfy the mass balance of the reaction, in which the dominant equilibrium gas species are assumed to evaporate, as in Imae et al. (1993). In Figure 7, the four models are depicted with the reactions at the surface of forsterite and the forsterite–enstatite interface. In model 1, Si diffuses from the forsterite–enstatite interface and evaporates at the forsterite surface through the reaction with forsterite, and Mg diffuses from the forsterite surface to the forsterite–enstatite interface to

Table 3. Summary of conditions and results of evaporation experiments in hydrogen gas.[a]

T (°C)	Time (hr)	c_0 (cm)	S (cm^2)	W_0 (g)	W_{after} (g)	ΔW (g)	F (%)	ΔWIS (g cm^{-2})
				$p(H_2) = 6.1 \times 10^{-6}$ bar				
1300	8	0.235	0.0821 (135)	0.00693	0.00638	0.00055	7.9	0.00670 (117)
1300	16	0.175	0.0969 (185)	0.00837	0.00767	0.00070	8.4	0.00722 (141)
1300	19	0.165	0.0655 (144)	0.00453	0.00388	0.00065	14.3	0.00992 (223)
1400	3	0.175	0.0713 (149)	0.00498	0.00437	0.00061	12.2	0.00855 (184)
1400	6	0.180	0.0560 (116)	0.00362	0.00302	0.00060	16.6	0.01072 (228)
1400	4	0.120	0.0449 (142)	0.00206	0.00166	0.00040	19.4	0.00891 (290)
1500	1	0.125	0.0605 (160)	0.00403	0.00351	0.00052	12.9	0.00859 (232)
1500	2	0.165	0.1357 (244)	0.01333	0.01165	0.00168	12.6	0.01238 (224)
1500	3	0.185	0.0738 (158)	0.00546	0.00415	0.00131	24.0	0.01775 (383)
				$p(H_2) = 2.0 \times 10^{-6}$ bar				
1300	11	0.260	0.0850 (136)	0.00528	0.00496	0.00032	6.1	0.00376 (70)
1300	18	0.170	0.0703 (144)	0.00384	0.00367	0.00017	4.4	0.00242 (66)
1300	25	0.260	0.1133 (166)	0.00845	0.00755	0.00090	10.7	0.00795 (120)
1400	3	0.165	0.0637 (144)	0.00331	0.00316	0.00015	4.5	0.00236 (72)
1400	9	0.140	0.0603 (161)	0.00373	0.00329	0.00044	11.8	0.00729 (201)
1400	16	0.170	0.0757 (170)	0.00516	0.00398	0.00118	22.9	0.01560 (353)
1500	1	0.130	0.0667 (161)	0.00387	0.00352	0.00035	9.0	0.00525 (135)
1500	2	0.108	0.0767 (202)	0.00472	0.00409	0.00063	13.3	0.00821 (220)
1500	4	0.190	0.0752 (148)	0.00498	0.00386	0.00112	22.5	0.01489 (296)
				$p(H_2) = 7.2 \times 10^{-7}$ bar				
1300	11	0.130	0.0336 (91)	0.00162	0.00157	0.00005	3.1	0.00149 (101)
1300	23	0.095	0.0343 (117)	0.00174	0.00167	0.00007	4.0	0.00204 (114)
1300	44	0.120	0.0302 (96)	0.00128	0.00109	0.00019	14.8	0.00630 (225)
1400	16	0.195	0.0521 (115)	0.00280	0.00238	0.00042	15.0	0.00805 (187)
1400	20	0.110	0.0544 (151)	0.00351	0.00329	0.00085	24.2	0.01561 (436)
1400	24	0.110	0.0507 (135)	0.00351	0.00279	0.00072	20.5	0.01421 (383)
1500	1	0.110	0.1089 (252)	0.00906	0.00883	0.00023	2.5	0.00211 (57)
1500	2	0.090	0.0621 (189)	0.00371	0.00346	0.00025	6.7	0.00402 (132)
1500	3	0.105	0.0338 (104)	0.00185	0.00165	0.00020	10.8	0.00592 (204)

[a] $p(H_2)$, hydrogen pressure; T, temperature; c_0, initial length of a prism along the c-axis; S, initial surface area of a sample (the area of the surface attached to a molybdenum box is excluded); W_0, initial weight of a sample; W_{after}, weight of a sample after heating; ΔW, weight loss; F, evaporated fraction.

form forsterite. In model 2, Si and O diffuse from the forsterite–enstatite interface and evaporate at the forsterite surface. In model 3, Si and O, which diffuse from the forsterite–enstatite interface, react with forsterite to evaporate, and Mg diffuses from the forsterite surface to the forsterite–enstatite interface and reacts with enstatite. Model 4 is unlikely as a reaction mechanism because the reaction at the surface of forsterite in model 4 is incongruent evaporation of forsterite, whereas the reactions in other models are those between forsterite and ions released from enstatite. The reaction in the model 4 is inconsistent with the fact that forsterite evaporates congruently. When we consider the volume change of formation of forsterite at the enstatite–forsterite boundary, as Imae et al. (1993) did, model 2 would be excluded because the volume change [$\Delta V = (V_{Fo} - V_{En})/V_{En}$] of -0.30 is much larger than others ($\Delta V = 0.05$ in model 1 and $\Delta V = -0.07$ in model 3). Although the comparison of volume change suggests that either model 1 or 3 is a plausible process, it seems to be difficult to determine diffusion species by the volume change alone.

The diffusion of species that has the slowest diffusion constant in forsterite should control the rate of the whole diffusion-controlled evaporation process. Diffusion of Mg in forsterite is $\sim 10^3$ to 10^7 times faster than that of O and Si in this experimental temperature range (Table 5), and therefore, diffusion of Mg is not the rate controlling process. It is unclear whether bulk diffusion of O is faster or slower than bulk diffusion of Si; Hallwig et al. (1982) reported the faster diffusion coefficient of silicon in forsterite than that of oxygen, whereas Jaoul et al. (1980, 1983) found that the diffusion of oxygen was much faster than that of silicon. Accordingly, we can only say that the rate controlling process is the bulk diffusion of O or Si in forsterite. The activation energy of κ_{En} (Eqn. 6) is close to that of bulk diffusion coefficients of Mg or O in forsterite (Table 5), although the possibility of diffusion of Si in the forsterite layer as the rate controlling process cannot be excluded because the uncertainty of the activation energy of κ_{En} is not so small (± 58 kJ/mol).

Because the forsterite layer is polycrystalline, grain boundary diffusion may control evaporation. However, in general, bulk diffusion tends to be the main transport mechanism at high temperatures rather than grain boundary diffusion because the activation energy of bulk diffusion is usually larger than that of grain boundary diffusion. We cannot discuss this further because there are few data for the temperature dependence of grain–boundary diffusion of Si and O in polycrystalline forsterite (e.g., Joeston, 1990) although there are data for Mg grain–boundary diffusion (Farver and Yund, 1994).

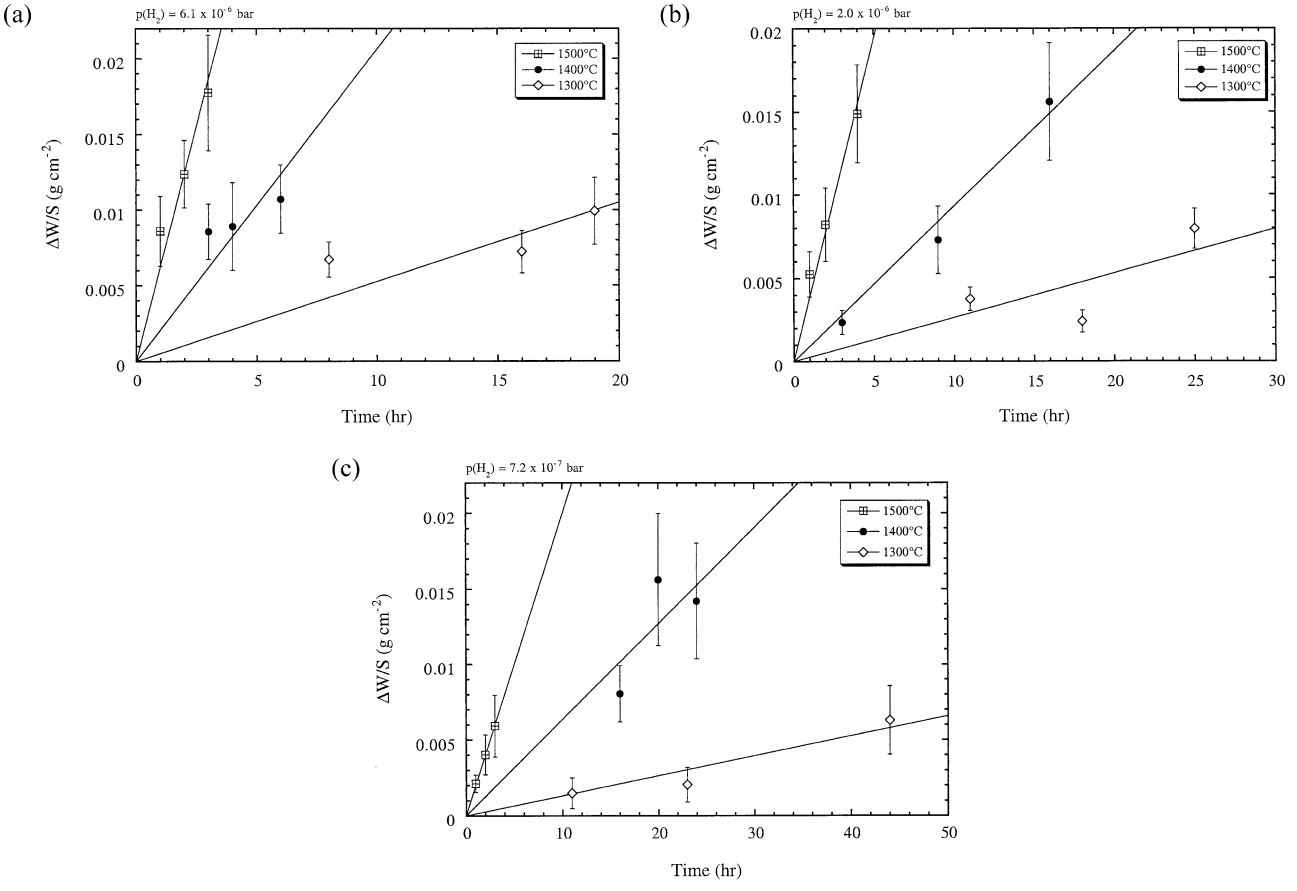

Fig. 5. The weight loss (g) per unit area (cm^2), $\Delta W/S$, of samples heated at 1500, 1400, and 1300°C in hydrogen gas. $\Delta W/S$ seems to be proportional to the heating duration. Linear fitting lines at 1500, 1400, and 1300°C are also shown. (a) $p(H_2) = 6.1 \times 10^{-6}$ bar. (b) $p(H_2) = 2.0 \times 10^{-6}$ bar. (c) $p(H_2) = 7.2 \times 10^{-7}$ bar. Errors are estimated from uncertainties of measurements of weight and surface area.

4.1.3. Evaporation in the Early Stage and Transition of Evaporation Modes

Evaporation of enstatite in the early stage of the heating experiments does not seem to be described by Eqn. 4 because this equation does not predict the peaks of X_{Fo} at 1500 and 1450°C (Figs. 3b,c). Also, X_{Fo} at 1400°C should achieve the steady state at $t > \sim 600$ h if Eqn. 4 is solved from $t = 0$ with κ_{En} (1400°C) in Table 4, which is inconsistent with experimental results (Fig. 3a). There must be other mechanisms to control evaporation in the early stage.

Evaporation of enstatite should be controlled by a surface

Table 4. The evaporation rate constants of enstatite and forsterite.[a]

T (°C)	κ_{En} ($cm^2\ s^{-1}$)	k_{Fo} ($cm\ s^{-1}$)
1400	$9.54\ (1.73) \times 10^{-13}$	$7.31\ (1.31) \times 10^{-10}$
1450	$3.00\ (0.48) \times 10^{-12}$	$2.58\ (0.37) \times 10^{-9}$
1500	$6.21\ (0.94) \times 10^{-12}$	$8.48\ (0.96) \times 10^{-9}$

[a] κ_{En}, diffusion-controlled evaporation rate constant of enstatite; k_{Fo}, evaporation rate constant of forsterite extrapolated from Hashimoto (1990).

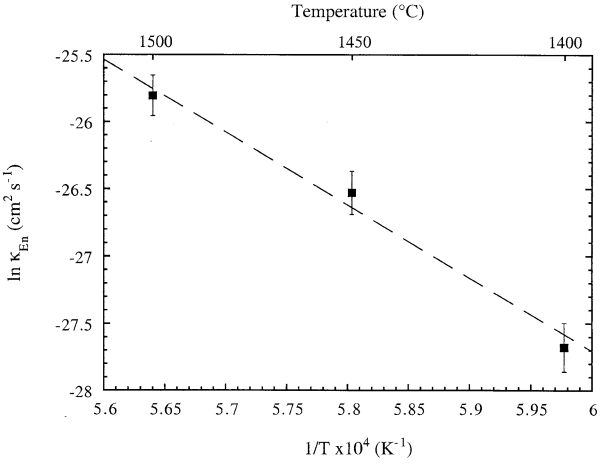

Fig. 6. Temperature dependence of the diffusion-controlled evaporation rate constant of enstatite, κ_{En}. The rate constant, κ_{En}, at each temperature is determined by the constant thickness of the forsterite layer in Figure 4 by using Eqn. 5. The data show the Arrhenius relation within experimental uncertainties. The activation energy of κ_{En} is 457 ± 58 kJ/mol. Errors are propagated from uncertainties of X_{Fo}.

(1)

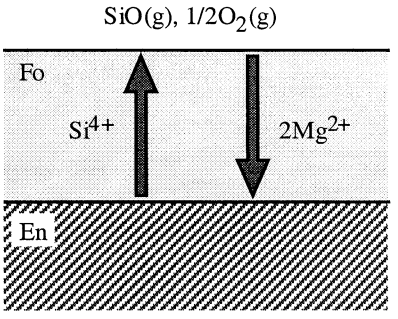

$Mg_2SiO_4 + Si^{4+} = 2Mg^{2+} + 2SiO(g) + O_2(g)$
(Reaction at the forsterite surface)

$4MgSiO_3 + 2Mg^{2+} = 3Mg_2SiO_4 + Si^{4+}$ (ΔV=0.05)
(Reaction at the interface between forsterite and enstatite)

(2)

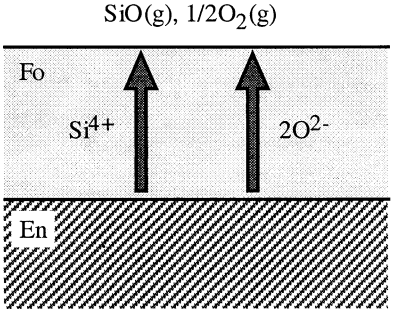

$Si^{4+} + 2O^{2-} = SiO(g) + 1/2O_2(g)$

$2MgSiO_3 = Mg_2SiO_4 + Si^{4+} + 2O^{2-}$ (ΔV=-0.30)

(3)

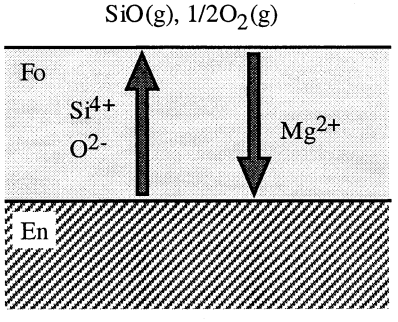

$Mg_2SiO_4 + 2Si^{4+} + 2O^{2-} = 2Mg^{2+} + 3SiO(g) + 3O_2(g)$

$6MgSiO_3 + 2Mg^{2+} = 4Mg_2SiO_4 + 2Si^{4+} + 2O^{2-}$ (ΔV=-0.07)

(4)

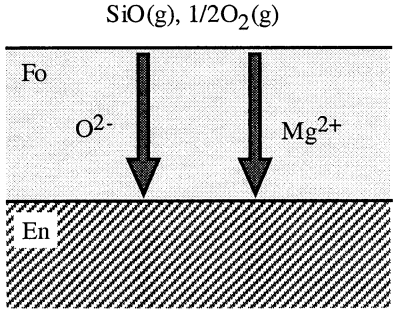

$Mg_2SiO_4 = 2Mg^{2+} + 2O^{2-} + SiO(g) + 1/2O_2(g)$

$2MgSiO_3 + 2Mg^{2+} + 2O^{2-} = 2Mg_2SiO_4$ (ΔV=+0.40)

Fig. 7. Schematic illustrations of four diffusion models for evaporation of enstatite and formation of forsterite to satisfy the mass balance of the reaction. Reactions at the forsterite surface and the interface between forsterite and enstatite are also shown: $\Delta V = (V_{Fo} - V_{En})/V_{En}$.

Table 5. Comparison of the activation energy of the diffusion-controlled evaporation rate constant, κ_{En}, with activation energies of bulk diffusion coefficients of ions in forsterite.[a]

E_a (kJ/mole)	D_0 (cm^2 s^{-1})	T (°C)	D at 1500°C (cm^2 s^{-1})	D at 1400°C (cm^2 s^{-1})	Reference
457 (58)	—	1400–1500	—	—	This study (κ_{En})
		^{16}O			
372 (13)	3.5×10^{-3}	1275–1630	3.79×10^{-14}	8.38×10^{-15}	1
323 (42)	5.6×10^{-3}	1150–1600	3.19×10^{-14}	8.62×10^{-15}	2
293 (42)	2.3×10^{-6}	1300–1600	5.31×10^{-15}	1.62×10^{-15}	3
475	1.6	1000–1510	1.60×10^{-14}	2.32×10^{-15}	4
		^{30}Si			
176	8.5×10^{-9}	1513–1723	5.52×10^{-14}	2.70×10^{-14}	4
377	1.5×10^{-6}	1325–1725	1.16×10^{-17}	2.51×10^{-18}	5
		^{26}Mg			
373	4.1	1373–1693	4.15×10^{-11}	9.14×10^{-12}	4
444	1.5×10^{3}	1300–1400	1.23×10^{-10}	2.02×10^{-11}	6
400 (60)	9.6	1000–1300	1.55×10^{-11}	3.07×10^{-12}	7

[a] E_a, activation energy; D_0, pre-exponential term; T, experimental temperature range.
References: 1: Reddy et al. (1980); 2: Jaoul et al. (1980); 3: Jaoul et al. (1983); 4: Hallwig et al. (1982); 5: Jaoul et al. (1981); 6: Morioka (1981); 7: Chakraborty et al. (1994).

reaction (evaporation of the SiO_2 component from enstatite and nucleation of forsterite) on the surface of enstatite in the very early stage of evaporation. After the surface is completely covered with forsterite, if the layer is still porous, enstatite beneath forsterite crystals can evaporate through the porous layer by the enstatite–forsterite interface diffusion, which would be faster than the bulk diffusion in forsterite. If such interface diffusion is an important mechanism for evaporation, the thickening rate of the forsterite layer is expressed by a similar equation to Eqn. 4. The thickness of the forsterite layer could in this case grow faster than the bulk diffusion-controlled evaporation (Eqn. 4) and become larger than the steady thickness expressed by Eqn. 5 because the diffusion rate constant through the enstatite–forsterite interface would be larger than κ_{En}.

Until the whole surface is covered with a compact forsterite layer due to grain growth, both the surface reaction-controlled evaporation and evaporation by the enstatite–forsterite interface diffusion would be the main mechanisms for evaporation of enstatite (formation of forsterite). It is difficult to make an evaporation model for the early stage by taking the above evaporation mechanisms into consideration because there are many unknown parameters such as the surface reaction-controlled and interface diffusion-controlled evaporation rate constants and the growth rate of forsterite on the surface.

The fact that X_{Fo} increases in the early stage of evaporation, then decreases and approaches the steady value (X^*_{Fo}) at 1500 and 1450°C (Fig. 4) could be explained by the transition of evaporation modes from the surface reaction- and interface diffusion–controlled evaporation to bulk diffusion controlled evaporation. We solved Eqn. 4 to reproduce the depletion patterns of X_{Fo} at 1500 and 1450°C by using κ_{En} and k_{Fo} in Table 4. It was assumed that the forsterite layer had become compact after heating for 90 and 110 h at 1500 and 1450°C, respectively, and the values of X_{Fo} of samples heated for 90

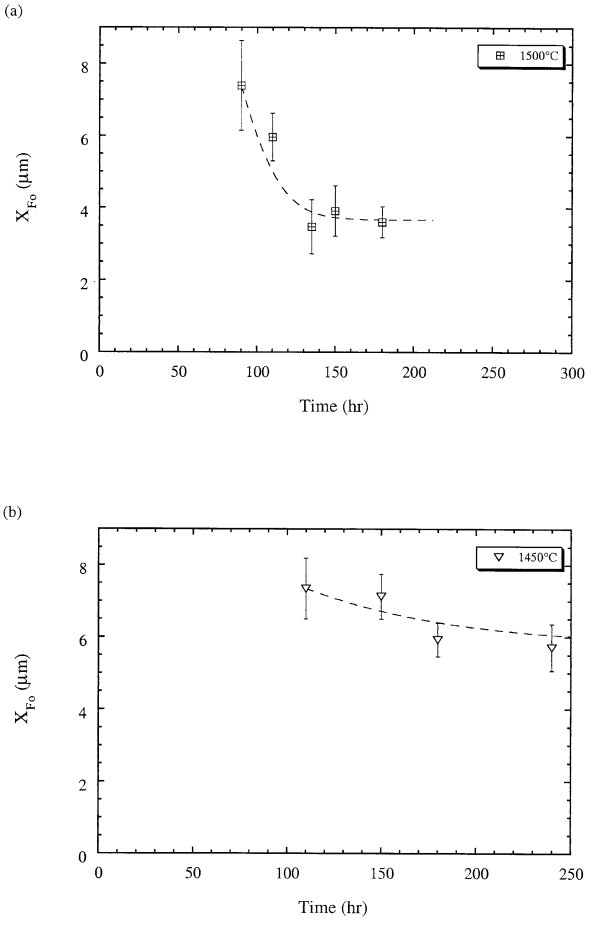

Fig. 8. X_{Fo} and X_{Fo}-t curves calculated from Eqn. 4. The values of κ_{En} of Eqn. 6 and k_{Fo} extrapolated from Hashimoto (1990) were used to solve Eqn. 4. The calculated X_{Fo} patterns reproduce the experimental depletion patterns of X_{Fo} well. (a) 1500°C. (b) 1450°C.

Table 6. Evaporation rate of enstatite in hydrogen gas.

T (°C)	J (g cm^{-2} s^{-1})
$p(H_2) = 6.1 \times 10^{-6}$ bar	
1300	$1.51\ (0.18) \times 10^{-7}$
1400	$5.85\ (0.82) \times 10^{-7}$
1500	$1.77\ (0.22) \times 10^{-6}$
$p(H_2) = 2.0 \times 10^{-6}$ bar	
1300	$6.29\ (0.74) \times 10^{-8}$
1400	$2.39\ (0.37) \times 10^{-7}$
1500	$1.13\ (0.16) \times 10^{-6}$
$p(H_2) = 7.2 \times 10^{-7}$ bar	
1300	$3.27\ (0.92) \times 10^{-8}$
1400	$1.59\ (0.24) \times 10^{-7}$
1500	$5.67\ (0.57) \times 10^{-7}$

and 110 h at 1500 and 1450°C were adopted as initial conditions to solve Eqn. 4. Calculated X_{Fo} depletion curves are shown in Figure 8, and the calculated curve at each temperature reproduces the experimental results. In particular, the drastic decrease of X_{Fo} at 1500°C is reproduced well. X_{Fo} at 1400°C has no peak but it reaches the steady state at an earlier time than the time predicted by Eqn. 4, which would be also explained by the transition of evaporation modes.

4.2. Evaporation Kinetics of Enstatite in Hydrogen Gas

Because evaporation of enstatite in hydrogen gas proceeds almost linearly with time (Fig. 5), we fitted the experimental data by using the following equation:

$$\frac{\Delta W}{S}(\text{g cm}^{-2}) = J(\text{g cm}^{-2}\,\text{s}^{-1})t, \qquad (7)$$

where J is the mass loss flux and t is time (Table 6).

Two explanations for the linear evaporation rate of enstatite in hydrogen gas are possible: (1) surface reaction-controlled evaporation of enstatite, or (2) the steady state of bulk diffusion-controlled evaporation, in which evaporation proceeds at the surface reaction-controlled evaporation rate of forsterite. In the first case, the formation rate of the forsterite (dX_{Fo}/dt) should be expressed by the difference between the surface reaction-controlled evaporation rates of enstatite (k_{En}) and forsterite (k_{Fo}). We calculated X_{Fo} from J, which was converted to the linear evaporation rate (cm s^{-1}) being divided by the average density of enstatite (3.209 g cm^{-3}; Carmichael, 1989) and forsterite (3.213 g cm^{-3}; Carmichael, 1989), and the evaporation rate of forsterite in hydrogen gas (Tsuchiyama et al., 1998). The results predict that the layer of the forsterite layer should reach more than several microns within the duration of experimental heating, which is inconsistent with the experimental results showing that only thin forsterite layers are found.

In the case of the second possibility, the residual forsterite layer should have a constant thickness given by Eqn. 5. The evaporation rate of forsterite in hydrogen gas is larger than that in vacuum because hydrogen molecules (or hydrogen atoms) promote evaporation of forsterite (Nagahara and Ozawa, 1996b; Hashimoto, 1998; Tsuchiyama et al., 1998, 1999),

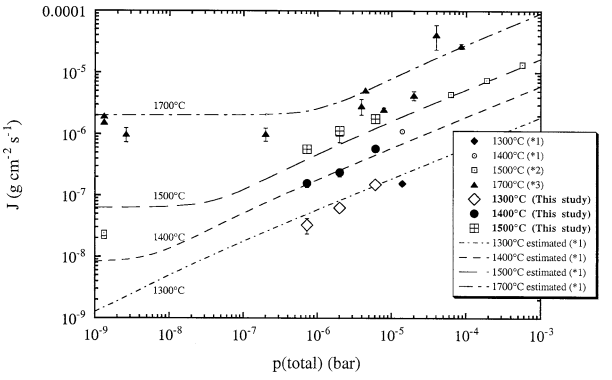

Fig. 9. Evaporation rates of forsterite estimated in the present study as a function of hydrogen pressure and temperature. Previous experimental evaporation rates of forsterite are also shown for comparison. 1, Tsuchiyama et al. (1998); 2, Hashimoto (1990, 1998); Wang et al. (1993, 1999) and Nagahara et al. (1997); 3, Nagahara and Ozawa (1996b). Broken curves show the evaporation rates of forsterite by Tsuchiyama et al. (1998) using theoretical evaporation rates and experimental data. Evaporation rates established in this study seem to be in good agreement with the evaporation rates of forsterite in previous studies.

whereas κ_{En} would have little dependence on hydrogen pressure. X^*_{Fo} in hydrogen gas, which is estimated from κ_{En} in Eqn. 4 and J, is in the range of 0.01 to 0.2 μm and much thinner than X^*_{Fo} in vacuum experiments. This is consistent with the experimental results, and a steady state would be achieved in experiments in hydrogen gas soon after evaporation started. The surface reaction-controlled evaporation rate of enstatite in hydrogen gas would also be enhanced in the presence of hydrogen gas. Thus, forsterite covers the whole enstatite surface within a short time because the nucleation rate of forsterite is increased by the enhanced evaporation rate of enstatite.

If evaporation achieves steady state, the value of J should correspond to the evaporation rate of forsterite. The temperature and hydrogen pressure dependence of J are shown in Figure 9 with evaporation rates of forsterite in previous experiments (Hashimoto, 1990, 1998; Wang et al., 1993, 1999; Nagahara and Ozawa, 1996b; Nagahara et al., 1997; Tsuchiyama et al., 1998). The evaporation rates of forsterite evaluated by Tsuchiyama et al. (1998) are also shown as broken lines in Figure 9. They compared experimental evaporation rates with theoretical ideal evaporation rates and concluded that evaporation rates of forsterite are almost one-tenth of the ideal evaporation rates. The dependence of J on temperature and hydrogen pressure is similar to that of evaporation rates of forsterite in hydrogen gas suggesting that J is equal to the evaporation rate of forsterite and that evaporation of enstatite in hydrogen gas proceeds in steady state at the evaporation rate of forsterite.

5. APPLICATION TO INCONGRUENT EVAPORATION OF ENSTATITE UNDER KINETIC CONDITIONS IN THE SOLAR NEBULA

If a Mg-rich evaporation residue (enstatite + forsterite) and Si-rich evaporated gas were formed as a result of incongruent evaporation of enstatite and if the two phases were subsequently separated from each other, Mg/Si fractionation would occur. We apply our experimental results to evaporation of

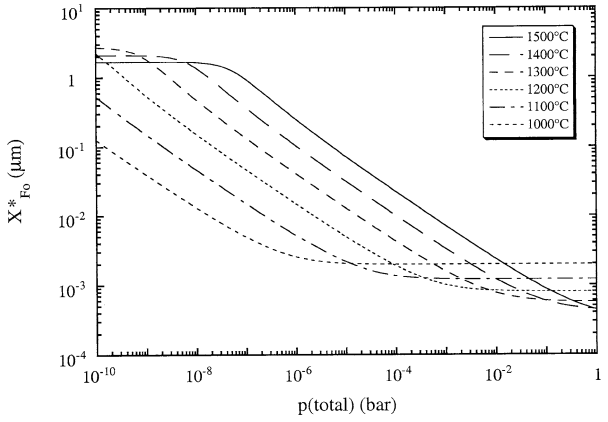

Fig. 10. The thickness of the forsterite layer for steady-state evaporation of enstatite, X^*_{Fo}, in an open system estimated as a function of temperature and total pressure in the primitive solar nebula. This gives the maximum thickness of the forsterite layer in the case of diffusion-controlled evaporation in an open system (Eqn. 5). Because diffusion processes in forsterite have little dependence on gas chemistry in the nebula, the diffusion-controlled evaporation rate constant obtained in this study is used as κ_{En} in the nebula. As for the evaporation rate of forsterite, the evaporation rate of forsterite evaluated by Tsuchiyama et al. (1999) is adopted. The figure indicates that only a thin forsterite layer would be formed by incongruent evaporation of enstatite because the evaporation rate of forsterite is enhanced in the presence of hydrogen gas in the nebula.

enstatite under solar nebula conditions and estimate the steady state thickness of the forsterite layer (X^*_{Fo}), which is the maximum thickness formed by diffusion-controlled evaporation except for the early transient stage.

X^*_{Fo} depends on the diffusion-controlled evaporation rate constant of enstatite (κ_{En}) and the surface reaction-controlled evaporation rate constant of forsterite (k_{Fo}) (Eqn. 5). Although diffusion of ions through the forsterite layer may have dependence on gas chemistry in the solar nebula, κ_{En} obtained in this study is used as κ_{En} in the solar nebula.

The evaporation rate of forsterite (k_{Fo}) in the solar nebula has to be evaluated, which depends strongly on gas pressure and chemistry in the nebula. We used the evaporation rates of forsterite of Tsuchiyama et al. (1999), who derived a value for k_{Fo} in the solar nebula by using experimental results and a quasi-equilibrium evaporation model (Kubaschewski et al., 1967). They proposed a new evaporation regime (H_2O/H_2 buffer dominated, or HBD) in addition to free evaporation dominated (FED) and hydrogen reaction-dominated (HRD) regimes, which were named by Richter and Davis (1997). Forsterite evaporates as in vacuum in the FED regime, whereas forsterite reacts with hydrogen to evaporate in the HRD regime. In the HBD regime, the evaporation rates of forsterite are determined only by the H_2O/H_2 ratio in the nebula and independent of hydrogen pressure in the nebula. This evaporation regime appears at high total pressures, low temperatures, or both (Tsuchiyama et al., 1999).

The estimated X^*_{Fo} in the nebula, which is obtained by a one-dimensional treatment (Eqn. 5), is shown in Figure 10. X^*_{Fo} at high temperatures and low nebular pressures is constant irrespective of the pressure because the evaporation regime of forsterite is FED. X^*_{Fo} at low temperatures and high pressures is also independent on the pressure, because the evaporation regime of forsterite is HBD. In the HRD regime that appears between FED and HBD, X^*_{Fo} decreases almost linearly with $p_{total}^{0.5}$ because the evaporation rate of forsterite in HRD increases almost linearly with $p_{total}^{0.5}$ ($\approx p_{H_2}{}^{0.5}$).

X^*_{Fo} in FED and HBD is larger at lower temperatures than at higher temperatures, whereas X^*_{Fo} in HRD is larger at higher temperatures than at lower temperatures. This is due to the difference in activation energies between κ_{En} (458 kJ/mol) and k_{Fo} in the three evaporation regimes (~600 kJ/mol in FED; ~300 kJ/mol in HRD; ~520 kJ/mol in HBD).

One can see from Figure 10 that X^*_{Fo} is less than 0.1 μm for evaporation in an open system, in which evaporated gases are taken away immediately, assuming the plausible range of the nebular total pressures (10^{-3}-10^{-6} bar). The possibility of Mg/Si fractionation by evaporation of enstatite depends on the grain size of enstatite particles. If the size of enstatite grains is much larger than X^*_{Fo}, the abundance ratio of forsterite to enstatite in a grain would be quite small and the Mg/Si ratio of the grain would not significantly differ from unity. In this case, Mg/Si fractionation would not be expected even if the solid–gas separation occurred. On the other hand, if an enstatite grain whose size is submicron evaporates, the forsterite layer formed on a grain would be comparable to the grain size and the Mg/Si ratio of the grain would become larger than the original ratio. Large variations of Mg/Si ratios between solid and gas would be expected in this case and Mg/Si fractionation would occur if the effective solid–gas separation took place. Because the typical size of interstellar dust particles that explains the observed interstellar extinction is submicron (e.g., Mathis et al., 1977) and presolar grains in primitive meteorites have the size ranging from submicron to 10 μm (e.g., Anders and Zinner, 1993), the size of dust grains in the early solar nebula would not be much larger than X^*_{Fo} in Figure 10 but comparable to X^*_{Fo}. Accordingly, evaporation of tiny enstatite grains under kinetic conditions in the solar nebula would play an important role in producing Mg/Si variations among different chemical groups of chondrites.

Our present results show that Mg/Si variations in solid and gas could be produced only by evaporation of submicron enstatite particles in the case of evaporation in an open system under solar nebula conditions. The situation, where evaporated gases are left around grains, may also have occurred in the solar nebula. The evaporation rate of residual forsterite would become smaller because of back reaction (recondensation) of ambient gas in this case. Because the evaporation behavior of enstatite would be different from the one in an open system, evaporation of enstatite in such a situation should also be investigated to study the possibility of Mg/Si fractionation by evaporation of enstatite in the solar nebula. It is also possible to evaluate the lifetime of enstatite grains, the time for equilibration in a closed system and the changes of Mg/Si ratios in solid and gas with time on the basis of experimental kinetics. Detailed applications will be presented elsewhere (Tachibana et al., in preparation).

Acknowledgments—We thank C. Koike and H. Chihara for FT-IR analyses of samples, K. Ozawa, G. Libourel, and M. Kitamura for useful discussion and advice, and J. B. Smith for reading the manuscript. We thank R. H. Nichols and R. Dohmen for constructive and

helpful reviews and H. Palme for careful reviews and editorial assistance. S.T. thanks the JSPS Research Fellowship for Young Scientists.

Associate editor: H. Palme

REFERENCES

Anders E. and Grevesse N. (1989) Abundance of the elements: Meteoritic and solar. *Geochim. Cosmochim. Acta* **53,** 197–214.

Anders E. and Zinner E. (1993) Interstellar grains in primitive meteorites: Diamond, silicon carbide, and graphite. *Meteoritics* **28,** 490–514.

Brealey A. J. and Jones R. H. (1998) Chondritic meteorites. In *Planetary Materials,* Vol. 36 of *Reviews in Mineralogy*(ed. J. J. Papike), pp. 3-01-3-398. Mineralogical Society of America.

Carmichael R. S. (1989) *Physical Properties of Rocks and Minerals.* CRC Press.

Chakraborty S., Farver J. R., Yund R. A., and Rubie D. C. (1994) Mg tracer diffusion in synthetic forsterite and San Carlos olivine as function of P, T, fO_2. *Phys. Chem. Mineral.* **21,** 489–500.

Cohen B. A., Hewins R. H., and Yu Y. (2000) Evaporation in the young solar nebula as the origin of 'just-right' melting of chondrules. *Nature* **406,** 600–602.

Dodd R. T. (1981) *Meteorites.* Cambridge University Press.

Farver J. R. and Yund R. A. (1994) Magnesium grain boundary diffusion in forsterite aggregates at 1000–1300°C and 0.1 MPa to 10 GPa. *J. Geophys. Res.* **99,** 19809–19819.

Grossman J. N. (1996) Chemical fractionation of chondrites: Signatures of events before chondrule formation. In *Chondrules and Protoplanetary Disk* (eds. R. H. Hewins, R. H. Jones and E. R. D. Scott), pp. 243–253. Cambridge University Press.

Grossman L. (1972) Condensation in the primitive solar nebula. *Geochim. Cosmochim. Acta* **36,** 597–619.

Hallwig D., Schactner R., and Sockel H. G. (1982) Diffusion of magnesium, silicon and oxygen in Mg_2SiO_4 and formation of the compound in the solid state. In *Reactivity of Solids* (ed. K. Dryek, J. Habor, and J. Nowotry), pp. 166–169. Proceedings of the 9th International Symposium. Elsevier Science.

Hashimoto A. (1983) Evaporation metamorphism in the early solar nebula—Evaporation experiments on the melt FeO-MgO-SiO_2-CaO-Al_2O_3. *Geochem. J.* **17,** 111–145.

Hashimoto A. (1990) Evaporation kinetics of forsterite and implications for the early solar nebula. *Nature* **347,** 53–55.

Hashimoto A. (1998) Absolute reaction rates of hydrogen with condensed phases in the nebula (abstract). *Meteor. Planet. Sci.* **33,** A65.

Hirth J. P. and Pound G. M. (1963) *Condensation and Evaporation, Nucleation and Growth Kinetics.* Pergamon Press.

Imae N., Tsuchiyama A., and Kitamura M. (1993) An experimental study of enstatite formation reaction between forsterite and Si-rich gas. *Earth Planet. Sci. Lett.* **118,** 21–30.

Ito J. (1975) High temperature solvent growth of orthoenstatite, Mg-SiO_3, in air. *Geophys. Res. Lett.* **2,** 533–536.

Jäger C., Molster F. J., Dorschner J., Henning Th., Mutschke H. and Waters L. B. F. M. (1998) Steps toward interstellar silicate mineralogy. IV. The crystalline revolution. *Astron. Astrophys.* **339,** 904–916.

Jaoul O., Froidevaux C., Durham W. B., and Michaut M. (1980) Oxygen self-diffusion in forsterite: Implication for the high temperature creep mechanism. *Earth Planet. Sci. Lett.* **47,** 391–397.

Jaoul O., Poumellec M., Froidevaux C., and Havette A. (1981) Silicon diffusion in forsterite: A new constraint for understanding mantle deformation. In *Anelasticity in the Earth* (eds. F. D. Stacey, M. S. Paterson, and A. Nicholas), pp. 95–100. Geodynamics Series 4. American Geophysics Union.

Jaoul O., Houlier B., and Abel F. (1983) Study of ^{18}O diffusion in magnesium orthosilicate by nuclear microanalysis. *J. Geophys. Res.* **88,** 613–624.

Joeston R. (1990) Grain–boundary diffusion kinetics in silicates and oxide minerals. In *Diffusion, Atomic Ordering, and Mass Transport: Selected Topics in Geochemistry,* Vol. 8 of *Advances in Physical Geochemistry*(ed. J. Ganguly), pp. 345–395. Springer Verlag.

Kallemeyn G. W. (1988) Elemental variations in bulk chondrites: A brief review. In *Meteorites and the Early Solar System* (eds. J. F. Kerridge and M. S. Matthews), pp. 390–393. University of Arizona Press.

Kerridge J. F. (1979) Fractionation of refractory lithophile elements among chondritic meteorites. *Proc. Lunar Planet. Sci. Conf.* **10,** 989–996.

Krot A. N., Fegley B. Jr., Lodders K., and Palme H. (2000) Meteoritical and astrophysical constraints on the oxidation state of the solar nebula. In *Protostars and Planets IV* (eds. V. Mannings, A. P. Boss, and S. S. Russel), pp. 1019–1054. Arizona Press.

Kubaschewski O., Evans E. Li., and Alcock C. B. (1967) *Metallurgical Thermochemistry.* Pergamon Press.

Kushiro I. and Mysen B. O. (1991) Experimental studies of the system Mg_2SiO_4-SiO_2-H_2 at pressures 10^{-2}–10^{-10} bar and at temperatures to 1650°C. In *Progress in Metamorphic and Magmatic Petrology* (ed. L. L. Perchuk), pp. 411–433. Cambridge University Press.

Larimer J. W. (1979) The condensation and fractionation of refractory lithophile elements. *Icarus* **40,** 446–454.

Larimer J. W. and Anders E. (1967) Chemical fractionation in meteorites—II. Abundance patterns and their interpretation. *Geochim. Cosmochim. Acta* **31,** 1239–1270.

Larimer J. W. and Anders E. (1970) Chemical fractionation in meteorites—III. Major element fractionations in chondrites. *Geochim. Cosmochim. Acta* **34,** 367–387.

Lewis J. S. (1972) Metal/silicate fractionation in the solar system. *Earth Planet. Sci. Lett.* **15,** 286–290.

Lewis J. S. and Prinn R. G. (1980) Kinetic inhibition of CO and N_2 reduction in the solar nebula. *Astrophys. J.* **238,** 357–364.

Lodders K. and Fegley B. Jr. (1999) *The Planetary Scientist's Companion.* Oxford University Press.

Mathis J. S., Rumpl W., and Nordsieck K. H. (1977) The size distribution of interstellar grains. *Astrophys. J.* **217,** 425–433.

Morioka M. (1981) Cation diffusion in olivine—II. Ni-Mg, Mn-Mg, Mg and Ca. *Geochim. Cosmochim. Acta* **45,** 1573–1580.

Nagahara H. and Ozawa K. (1996a) Evaporation of silicate melt in the system Mg_2SiO_4-SiO_2 (abstract). *Antarctic Meteor.* **21,** 125–127.

Nagahara H. and Ozawa K. (1996b) Evaporation of forsterite in H_2 gas. *Geochim. Cosmochim. Acta* **60,** 1445–1459.

Nagahara H., Ozawa K., and Morioka M. (1997) Anisotropy of evaporation of forsterite (II): Temperature dependence of kinetics. *Proc. Japan Earth Planet. Sci. Joint Mtng.* 505.

Nagahara H. and Ozawa K. (1999) Mechanism of forsterite evaporation as inferred from surface microstructure. *Proc. Jpn. Acad.* **75,** 29–34.

Nichols R. H. Jr., Grimley R. T., and Wasserburg G. J. (1998) Measurement of gas-phase species during Langmuir evaporation of forsterite (abstract). *Meteor. Planet. Sci.* **33,** A115–A116.

Ozawa K. and Nagahara H. (2000) Kinetics of diffusion-controlled evaporation of Fe-Mg olivine: Experimental study and implication for stability of Fe-rich olivine in the solar nebula. *Geochim. Cosmochim. Acta* **64,** 939–955.

Ozima M. (1982) Growth of orthoenstatite crystals be the flux method. *J. Jpn. Assoc. Mineral. Petrol. Econ. Geol. (Suppl).* **3,** 97–103 (in Japanese).

Petaev M. I. and Wood J. A. (1998) The condensation with partial isolation (CWPI) model of condensation in the solar nebula. *Meteoritics and Planet. Sci.* **33,** 1123–1137.

Reddy K. P. R., Oh S. M., Major L. D. Jr., and Cooper A. R. (1980) Oxygen diffusion in forsterite. *J. Geophys. Res.* **85,** 322–326.

Richter F. M. and Davis A. M. (1997) Mass loss kinetics and isotope fractionation of type B CAI melts at 1400°C and solar f_{O_2} (abstract). *Lunar Planet. Sci.* **28,** 1161–1162.

Rietmeijer F. J. M. (1998) Interplanetary dust particles. In *Planetary Materials,* Vol. 36 of *Reviews in Mineralogy* (ed. J. J. Papike), pp. 2-01-2-95. Mineralogical Society of America.

Sears D. W. G. and Weeks K. S. (1986) Chemical and physical studies of type 3 chondrites—VI. Siderophile elements in ordinary chondrites. *Geochim. Cosmochim. Acta* **50,** 2815–2832.

Sears D. W. G. and Dodd R. T. (1988) Overview and classification of meteorites. In *Meteorites and the Early Solar System* (eds. J. F. Kerridge and M. S. Matthews), pp. 3–31. University of Arizona Press.

Sears D. W. G., Huang S., and Benoit P. H. (1996) Open-system behaviour during chondrule formation. In *Chondrules and Proto-*

planetary Disk (eds. R. H. Hewins, R. H. Jones and E. R. D. Scott), pp. 221–231. Cambridge University Press.

Smith J. R. (1975) Experimental study on the polymorphism of enstatite. *Am. Mineral.* **59,** 345–352.

Tedmon C. S. Jr. (1966) The effect of oxide volatilization on the oxidation kinetics of Cr and Fe-Cr alloys. *J. Electrochem. Soc.* **113,** 766–768.

Tsuchiyama A., Takahashi T., and Tachibana S. (1998) Evaporation rates of forsterite in the system Mg_2SiO_4-H_2. *Mineral. J.* **20,** 113–126.

Tsuchiyama A., Tachibana S., and Takahashi T. (1999) Evaporation of forsterite in the primordial solar nebula; rates and accompanied isotopic fractionation. *Geochim. Cosmochim. Acta* **63,** 2451–2466.

Waelkens C., Waters L. B. F. M., de Graauw M. S., Huygen E., Malfait K., Plets H., Vandenbussche B., Beintema D. A., Boxhoorn D. R., Habing H. J., Heras A. M., Kester D. J. M., Kester D. J. M., Lahuis F., Morris P. W., Roelfsema P. R., Salama A., Siebenmorgen R., Trams N. R., van der Bliek N. R., Valentijn E. A., and Wesselius P. R. (1996) SWS observations of young main-sequence stars with dusty circumstellar disks. *Astron. Astrophys.* **315,** L245–L248.

Wai C. M. and Wasson J. T. (1977) Nebular condensation of moderately volatile elements and their abundances in ordinary chondrites. *Earth Planet. Sci. Lett.* **36,** 1–13.

Wang J., Davis A. M., Hashimoto A., and Clayton R. N. (1993) Diffusion-controlled magnesium isotopic fractionation of a single crystal forsterite evaporated from the solid state. *Lunar Planet. Sci.* **24,** 1479–1480.

Wang J., Davis A. M., Clayton R. N., and Hashimoto A. (1999) Evaporation of single crystal of forsterite: Evaporation kinetics, magnesium isotope fractionation, and implications of mass-dependent isotopic fractionation of a diffusion-controlled reservoir. *Geochim. Cosmochim. Acta* **63,** 953–966.

Wang J., Davis A. M., Clayton R. N., Mayeda T. K., and Hashimoto A. (2001) Chemical and isotopic fractionation during the evaporation of the FeO-MgO-SiO_2-CaO-Al_2O_3-TiO_2 rare earth element melt system. *Geochim. Cosmochim. Acta* **65,** 479–494.

Wasson J. T. and Chou C.-L. (1974) Fractionation of moderately volatile elements in ordinary chondrites. *Meteoritics* **9,** 69–84.

Wasson J. T. and Kallemeyn G. W. (1988) Compositions of chondrites. *Phil. Trans. R. Soc. Lond.* **A325,** 535–544.

Waters L. B. F. M., Molster F. J., de Jong T., Beintema D. A., Waelkens C., Boogert A. C. A., Boxhoorn D. R., de Graauw Th., Drapatz S., Feuchtgruber H., Genzel R., Helmivh F. P., Heras A. M., Huygen R., Izumiura H., Justtanont K., Kester D. J. M., Kunze D., Lahuis F., Lamers H. J. G. L. M., Leech K. J., Loup C., Lutz D., Morris P. W., Price S. D., Roelfsema P. R., Salama A., Schaeidt S. G., Tielens A. G. G. M., Trams N. R., Valentijn E. A., Vandenbussche B., van der Ancker M. E., van Dishoeck E. F., van Winckel H., Wesselius P. R., and Young E. T. (1996) Mineralogy of oxygen-rich dust shells. *Astron. Astrophys.* **315,** L361–L364.

Wood J. A. and Hashimoto A. (1993) Meniral equilibrium in fractionated nebular systems. *Geochim. Cosmochim. Acta* **57,** 2377–2388.